Metal-Adsorbate Interactions Modulate Plasmonic Reactivity of Chemisorbed Nitrophenyl Derivatives

*Kexun Chen and Hui Wang**

Department of Chemistry and Biochemistry, University of South Carolina, Columbia, South Carolina 29208, United States

* Corresponding author.

Email: *wang344@mailbox.sc.edu*; Phone: 1-803-777-2203; orcid.org/0000-0002-1874-5137.

ABSTRACT

Energetic hot electrons generated upon non-radiative decay of localized plasmons in metallic nanostructures can be effectively harnessed to catalyze photochemical transformations of molecular adsorbates through unique reaction pathways. When designing metal-adsorbate hybrid systems for hot electron-driven photocatalysis, both the intrinsic plasmonic properties of metallic photocatalysts and the chemical nature of metal-adsorbate interactions should be taken into careful considerations. In this work, we show that the reactivity of nitrophenyl derivative adsorbates on Ag nanoparticle surfaces toward plasmon-driven reductive coupling reactions is intimately tied to the bonding nature of molecular chemisorption. We focus on the comparative studies of three representative nitrophenyl derivatives, specifically *para*-nitrothiophenol, *para*-nitrophenylacetylene, and *para*-nitrophenylisocyanide, which covalently interact with the Ag photocatalysts using chemically distinct surface-anchoring groups. Taking full advantage of the unique time-resolving and molecular fingerprinting capabilities offered by surface-enhanced Raman spectroscopy, we have been able to precisely correlate the chemical nature of metal-adsorbate interactions to the kinetic characteristics of molecular transformations under a broad range of reaction conditions. Although the kinetic features of the coupling reactions change substantially upon variation of the excitation wavelength, the light illumination power, and the pH of the reaction medium, we have consistently observed that the plasmonic reactivity of the nitrophenyl derivative adsorbates drops drastically, as reflected by significant decrease in both reaction rates and yields, when the bonding modes dominating the metal-adsorbate interactions are switched from σ-donation to π-back donation.

KEYWORDS: plasmon resonance, plasmon-driven photocatalysis, hot electrons, surface-enhanced Raman scattering, metal-adsorbate interactions

INTRODUCTION

Optically excited metallic nanostructures may function as robust photocatalysts triggering plasmon-mediated interfacial molecule-transforming processes that are mechanistically distinct from the catalytic reactions under thermal conditions.[1-16] The plasmonic hot electrons, which are non-thermally distributed above the Fermi level of the metals, can be injected into unpopulated molecular orbitals of surface adsorbates to induce a series of intriguing bond-breaking and bond-forming photochemical reactions.[3-9] The photoexcitation efficiency, the lifetime of plasmonic electron oscillations, the energy distribution of hot electrons, and the electronic band energies of the coupled metal-adsorbate systems are all critical factors profoundly influencing the efficiency of hot electron injection into the molecular adsorbates. The photoexcitation, metal-to-adsorbate transfer, and thermal relaxation of hot electrons are all ultrafast photophysical processes on the femtosecond to nanosecond time-scales.[5, 6, 17] However, hot electron-driven photocatalysis, in many cases, involves drastically slower photochemical transformations spanning the time-scales from milliseconds to minutes,[5, 6, 10] implying that the rate-limiting kinetic bottle-necks are most likely associated with photo-induced chemical transformations of molecular adsorbates rather than photoexcitation and injection of hot electrons. In this work, we show that the plasmonic reactivity of molecular adsorbates is intimately tied to the chemical nature of metal-adsorbate interactions through a detailed case study of the reductive coupling of nitrophenyl derivatives chemisorbed to Ag nanoparticle surfaces.

In the ever-expanding family of plasmon-driven photoreactions, the reductive coupling of *para*-nitrothiophenol (pNTP) has become a model reaction ideal for detailed mechanistic studies of plasmon-mediated surface chemistry.[18-20] Plasmon-enhanced Raman spectroscopies, including both surface-enhanced Raman scattering (SERS) and tip-enhanced Raman scattering (TERS), have been utilized as surface-sensitive spectroscopic tools to precisely characterize the detailed structural evolution of molecular adsorbates during plasmon-driven photocatalytic reactions.[20-26] As revealed by SERS- and TERS-based spectroscopic studies, chemisorbed pNTP molecules undergo plasmon-driven reductive coupling reactions to produce *p,p′*-dimercaptoazobenzene (DMAB) on the surfaces of a diverse range of metallic nanostructures,[18-20, 27-42] providing a paradigm-shifting strategy for synthesizing aromatic azo compounds. However, the kinetic features and reaction pathways vary substantially from case to case, depending sensitively on the intrinsic properties of the metallic nanocatalysts (materials compositions, plasmon resonance frequencies, local-field enhancements, and surface structures), the photoexcitation conditions (excitation wavelength, excitation power density, and light illumination geometry), and the local environment in which the reactions occur (local temperature, pH, and presence of charge carrier acceptors). Several critical aspects of the detailed reaction mechanisms, such as the rate-limiting elementary steps,[29, 33, 38, 40] the exact roles of plasmonic photothermal heating,[28, 37, 41] and the relationship between reaction rates and local-field enhancements,[27, 38] are still under vibrant debate and remain open to further scrutiny. The seemingly divergent kinetic results and perplexing mechanistic characteristics reported in the literature strongly suggest that the plasmonic reactivity of pNTP adsorbates is not only related to the plasmon-derived photophysical effects but may also be modulated by the chemical interactions between the molecular adsorbates and the plasmonic photocatalysts. The metal-adsorbate interactions rigorously dictate the surface-orientation, structural ordering, and conformational flexibility of the chemisorbed molecules, all of which have been recently found to be key factors affecting the reactivity of thiolated nitrophenyl adsorbates toward the plasmon-driven reductive coupling reactions.[30, 42, 43]

While the thiolated molecules represent so far the most intensively studied chemisorbates on metal surfaces,[44] organic molecules may also use other non-thiolated surface-anchoring groups, such as diazonium,[45-50] terminal alkyne,[51-56] N-heterocyclic carbene,[57-62] and isocyano groups,[63-69] to form covalent interactions with metallic substrates. Previous studies of plasmon-driven nitro-coupling reactions, however, have been exclusively focusing on thiolated nitrophenyl adsorbates.[18-25, 27-43] How the non-thiolated nitrophenyl derivatives behave differently from their thiolated counterparts during the plasmon-driven coupling reactions remains unexplored yet. Here we systematically compare the plasmonic reactivity and transforming kinetics of pNTP, *para*-nitrophenylacetylene (pNPA), and *para*-nitrophenylisocyanide (pNPI), which chemisorb to Ag nanoparticle surfaces using the thiol, ethynyl, and isocyano groups, respectively. The chemical structures of the three nitrophenyl derivatives and the azo molecules produced through the plasmon-driven coupling reactions are shown in Scheme 1. Thiolated molecules are covalently bound to Ag surfaces through σ-donation of the lone-pair electrons of S to Ag, whereas the Ag-ethynyl interactions involve the contributions of both σ-donation and π-back donation. The σ-component is associated with the overlap between the conduction band of Ag and the π orbital of the ethynyl group, whereas the π-component arises from the electron back donation from the Ag valence band to the ethynyl π* orbital.[53-55] A particularly interesting discovery made in this work is that chemisorption of pNPI involves unique pH-dependent bimodal interactions between the isocyano group and the Ag surfaces, exhibiting the characteristics of the σ-donation mode in an acidic environment but becoming dominated by the π-back donation mode in an alkaline environment. Employing SERS as a molecular fingerprinting tool enables us not only to fully capture the essential spectral features reflecting the bonding nature of the Ag-adsorbate interactions, but also to precisely monitor the plasmon-mediated molecule-transforming processes in real time. The results of SERS-based kinetic measurements conducted under deliberately controlled reaction conditions provide important mechanistic insights into how the metal-adsorbate interactions modulate the plasmonic reactivity of the molecular adsorbates on nanostructured metal surfaces.

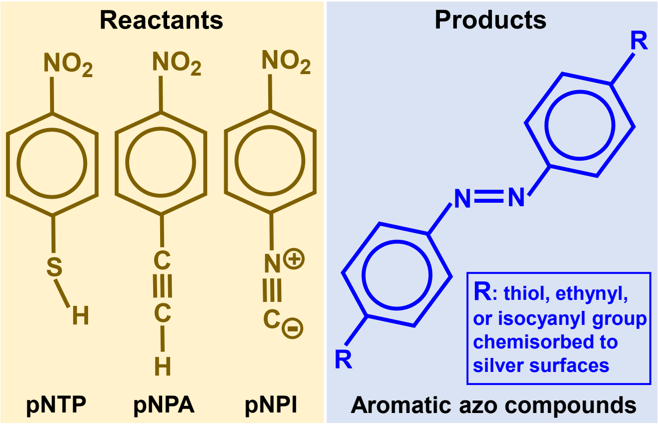

Scheme 1. Chemical structures of pNTP, pNPA, pNPI, and the aromatic azo compounds produced through the plasmon-driven reductive coupling reactions.

METHODS

Colloidal Ag nanoparticles with an average size of 44 nm were synthesized through seed-mediated nanocrystal growth employing cetyltrimethylammonium chloride (CTAC) as the surface-capping ligands.[70] Detailed description of the synthetic protocol was presented in the Supporting Information. A saturated monolayer coverage of chemisorbed nitrophenyl derivatives on the Ag nanoparticle surfaces was achieved through ligand exchange after incubating the CTAC-capped Ag nanoparticles with 10 mM of pNTP, pNPA, or pNPI (dissolved in 1:1 volume ratio of water and ethanol) at 40 ^{o}C for 2 h. Colloidal Ag nanoparticles coated with various nitrophenyl derivative adsorbates were centrifuged, redispersed in water, and finally assembled into close-packed arrays by slowly drying droplets of colloidal inks on indium tin oxide (ITO)-coated glass substrates at room temperature. The colloidal Ag nanoparticles and the nanoparticle array structures were characterized by scanning electron microscopy (SEM), transmission electron microscopy (TEM), and optical extinction spectroscopy, as detailed in the Supporting Information.

In this work, the as-assembled Ag nanoparticle arrays played a dual role as both the SERS substrates and the plasmonic photocatalysts. SERS spectra were collected using a BaySpec Nomadic^{TM} confocal Raman microscope built on an Olympus BX51 reflected optical system. Two continuous wave (cw) lasers with emission wavelengths of 532 and 785 nm were used as the excitation sources for both SERS and photocatalysis. The excitation lasers were focused onto a spot size of 2 μm in diameter in the focal plane using a 50× dark field objective (NA = 0.5, WD = 10.6 mm, Olympus LMPLFLN-BD), and the same objective was also used to collect the Raman signals in a back scattering configuration. The laser power focused onto the samples was adjusted either using neutral density filters or by changing the power output of the lasers. The integration time for spectral acquisition was typically in the range of 0.3-1 s. A homebuilt reaction chamber[71] was assembled on top of the ITO-supported Ag nanoparticle arrays, and was filled with an aqueous solution of either 5 mM H_2SO_4 (pH = 2) or 10 mM KOH (pH = 12) to control the pH of the reaction medium. The reaction progress was tracked in real time by collecting the temporally evolving SERS spectra under continuous laser illumination during the plasmon-driven coupling reactions.

Density functional theory (DFT) calculations were carried out using QChem 5.4 software package, with the functional of B3LYP applied in all simulations. The 6-31+G** basis set was used for all the non-metal atoms in the molecules, while the def2-ecp basis set was used for the Ag atoms and their effective core potential. More details of DFT calculations were described in the Supporting Information.

RESULTS AND DISCUSSION

Ag nanoparticles served as both the adsorbents for molecular chemisorption and the building blocks for the assembly of nanoparticle arrays. The as-synthesized Ag nanoparticles were quasi-spherical in shape with particle diameters narrowly distributed around 44 nm (Figures S1A and S1B in the Supporting Information). Colloidal Ag nanoparticles suspended in water displayed a well-defined light extinction peak centered at the wavelength of 415 nm (Figures S1C in the Supporting Information), which was the spectral signature of the dipole plasmon resonance of the nanoparticles. The CTAC ligands on the surfaces of the as-synthesized Ag nanoparticles could be fully displaced by pNTP, pNPA, and pNPI through ligand exchange. Aqueous colloidal inks containing nitrophenyl derivative-coated Ag nanoparticles underwent a slow solvent evaporation process on hydrophobic substrates, such as ITO-coated glass slides, to form close-packed arrays with sub-10 nm interparticle gaps (Figure 1A). The strong plasmon coupling among the neighboring nanoparticles resulted in a broad-band plasmonic feature spanning the entire visible and much of the near-infrared in the extinction spectrum (Figure 1B). Optical excitations of the broad-band plasmons by a visible (532 nm, 2.33 eV) or a near-infrared (785 nm, 1.58 eV) laser led to large local-field enhancements inside the interparticle gaps, which served as the hot spots for both Raman signal amplification and plasmonic photocatalysis. The SERS spectral features were essentially dominated by the Raman signals of the molecular adsorbates residing in the hot spots confined within the interparticle gaps. Upon complete ligand exchange, all the SERS features of CTAC, especially the strong peak of the Ag-Cl stretching mode (v_{AgCl}) at 245 cm^{-1}, completely disappeared, while the spectral signatures of the nitrophenyl derivatives became well-resolved in the SERS spectra (Figure S2 in the Supporting Information). The emergence of the characteristic Raman peaks of the Ag-S stretching (v_{AgS}) and Ag-C stretching (v_{AgC}) modes at ~ 328 and ~ 404 cm^{-1}, respectively, indicated that pNTP, pNPA, and pNPI were all chemisorbed to the Ag surfaces through covalent interactions.

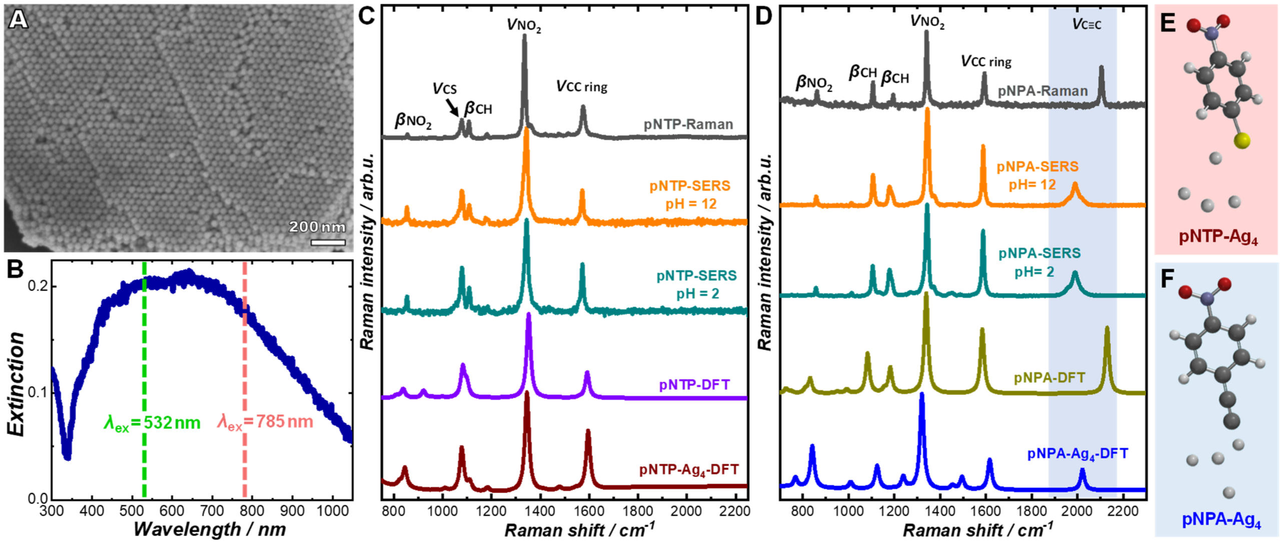

Figure 1. (A) SEM image and (B) extinction spectrum of pNPA-coated Ag nanoparticle arrays on an ITO-coated glass substrate. The wavelengths of the excitation lasers used for the SERS measurements are labeled with vertical dash lines in panel B. Experimentally measured normal Raman and SERS spectra and DFT-calculated Raman spectra of (C) pNTP and (D) pNPA. The normal Raman spectra were collected from solid samples of the molecules at a λ_{ex} of 785 nm and a P_{ex} of 6.44 mW with a spectral integration time of 20 s. The SERS spectra were collected from the molecular adsorbates on Ag nanoparticle arrays in acidic (pH of 2) and alkaline (pH of 12) aqueous media at a λ_{ex} of 785 nm and a P_{ex} of 0.29 mW with a spectral integration time of 5 s. The calculated Raman spectra of pNTP, pNTP-Ag$_4$, pNPA, and pNPA-Ag$_4$ are also shown for comparison with the experimentally measured spectra. The assignments of several major Raman peaks are labeled. Molecular structures optimized by DFT for (E) pNTP-Ag$_4$ and (F) pNPA-Ag$_4$.

Careful analysis of the SERS spectral features enabled us to extract detailed information concerning the molecular structures of the adsorbates and the chemical nature of the Ag-adsorbate interactions. In Figure 1C, we compare the SERS spectra collected from pNTP adsorbates on the Ag nanoparticle arrays to the normal Raman spectrum of neat pNTP at an excitation wavelength (λ_{ex}) of 785 nm. To eliminate the plasmon-driven coupling reactions, the SERS spectra were collected at a low excitation power (P_{ex}) of 0.29 mW within a spectral integration time of 5 s. Several characteristic vibrational modes of pNTP, including the benzene ring mode ($\nu_{CC\ ring}$, 1576 cm^{-1}), the nitro stretching mode (ν_{NO2}, 1334 cm^{-1}), the C-S stretching mode (ν_{CS}, 1076 cm^{-1}), the nitro scissoring mode (β_{NO2}, 856 cm^{-1}), and the C-H bending mode (β_{CH}, 1105 cm^{-1}), were clearly resolved in the normal Raman spectrum. All these vibrational modes were also well-reproduced in the SERS spectra of chemisorbed pNTP. The structures of pNTP chemisorbed on Ag appeared pH-independent, giving rise to essentially the same SERS spectral features in acidic (pH = 2) and alkaline (pH = 12) environments. The ν_{CS} mode in the SERS spectra remained unshifted in comparison to that in the normal Raman spectrum, indicating that the formation of Ag-S covalent bond introduced negligible modification of the length and order of the C-S bond in pNTP. As shown in Figure 1D, the SERS features of chemisorbed pNPA also matched the normal Raman features of neat pNPA very well, except that the C≡C stretching ($\nu_{C\equiv C}$) mode in the SERS spectra was downshifted by ~113 cm^{-1} (from ~2105 cm^{-1} in normal Raman spectrum to ~1992 cm^{-1} in SERS spectra) and became significantly broadened in comparison to that in the normal Raman spectrum. The spectral downshift and lineshape broadening of the $\nu_{C\equiv C}$ mode were essentially caused by the π-back donation of electrons form the Ag valence band to the antibonding π* orbital of the terminal alkyne. The experimental results were further corroborated by DFT calculations, which not only confirmed the Raman peak assignments but also provided insights into the origin of the spectral shift of the $\nu_{C\equiv C}$ mode. We calculated the Raman spectra of pNTP-Ag_4 and pNPA-Ag_4 compounds, which were composed of an Ag_4 atomic cluster covalently linked to pNTP and pNPA through Ag-S and Ag-C bonds, respectively. The chemical structures of pNTP-Ag_4 and pNPA-Ag_4 optimized by DFT are shown in Figure 1E and 1F, respectively. The calculated Raman shifts of all the major vibration modes were in very good agreement with the experimental results (Figures 1C and 1D). According to the DFT results, the $\nu_{C\equiv C}$ mode of pNPA was downshifted by 106 cm^{-1} upon chemisorption to Ag due to the π-back donation effect associated with the Ag-ethynyl interactions.

pNTP and pNPA adsorbates exhibited strikingly different levels of reactivity toward the plasmon-driven coupling reactions, as evidenced by the results of time-resolved SERS measurements. Figure 2 shows the time-resolved SERS spectra collected from pNTP and pNPA on the Ag nanoparticle arrays during the coupling reactions at pHs of 2 and 12 under continuous illuminations by a 532 nm laser at a P_{ex} of 1.74 mW and by a 785 nm laser at a P_{ex} of 2.64 mW. In the time-resolved SERS spectra, the intensities of the spectroscopic signals were shown as the detected counts normalized against the spectral integration time and the excitation laser power, carrying the unit of counts per second per milliwatts (cps mW^{-1}). During the coupling reactions, the intensities of the ν_{NO2} and β_{NO2} modes progressively decreased, while several SERS peaks signifying the azo products, such as the C-N stretching mode (ν_{CN}, 1146 cm^{-1}) and the vibrational modes of the azo bond (ν_{NN}, 1438 and 1393 cm^{-1}), emerged and became gradually more intense. Therefore, the reaction progress could be tracked in real time based on the temporal evolution of the SERS spectral features. We used DFT to calculate the Raman spectra of the azo products, *p,p′*-dimercaptoazobenzene (DMAB) for pNTP coupling and *p,p′*-diynylazobenzene (DYAB) for pNPA coupling reactions, respectively (Figure S3 in the Supporting Information). Comparison of the experimental spectra to the DFT results clearly showed that the DMAB and DYAB molecules produced through the plasmon-driven coupling reactions adopted the thermodynamically favored *trans*-conformation rather than the meta-stable *cis*-conformation.

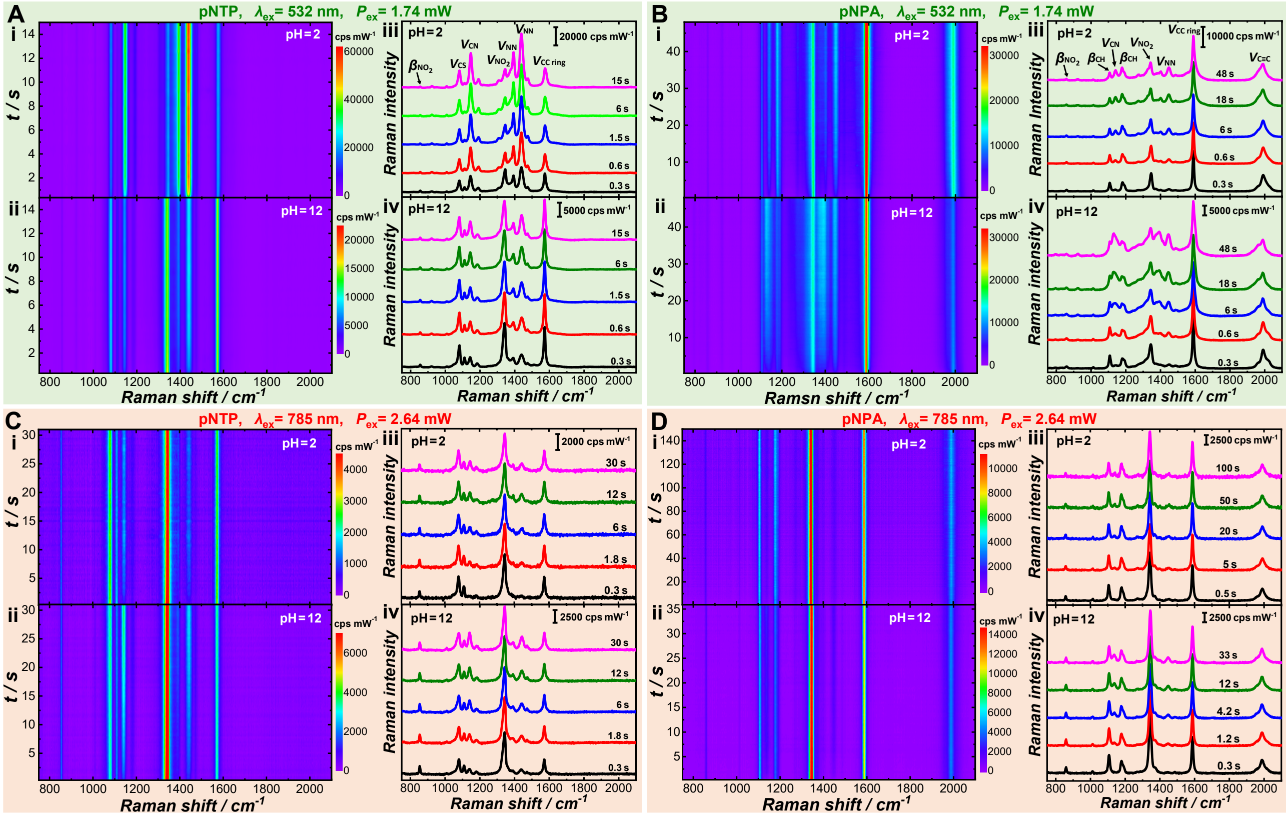

Figure 2. Time-resolved SERS spectra at pHs of (i) 2 and (ii) 12 and snap-shot SERS spectra captured at various reaction times at pHs of (iii) 2 and (iv) 12 for (A) pNTP at λ_{ex} of 532 nm and P_{ex} of 1.74 mW, (B) pNPA at λ_{ex} of 532 nm and P_{ex} of 1.74 mW, (C) pNTP at λ_{ex} of 785 nm and P_{ex} of 2.64 mW, and (D) pNPA at λ_{ex} of 785 nm and P_{ex} of 2.64 mW.

Several interesting observations are particularly noteworthy. First, both pNTP and pNPA were observed to be substantially more reactive at λ_{ex} of 532 nm than at λ_{ex} of 785 nm. Our DFT calculations showed that the lowest unoccupied molecular orbital (LUMO) of pNTP chemisorbed to Ag were located 1.9 eV above the Fermi level of Ag (Figure S4 in the Supporting Information), in agreement with previously calculated results.[72] At the λ_{ex} of 532 nm, a fraction of the photoexcited hot electrons were energetic enough to get injected into the LUMO of chemisorbed pNTP to initiate the reductive coupling reactions. At the λ_{ex} of 785 nm, however, the hot electrons became energetically insufficient for the Ag-to-pNTP transfer, and the reaction mechanism switched to an alternative pathway mediated by the molecular oxygen dissolved in water. The hot electrons were injected into molecular oxygen to produce anionic O_2^- species capable of inducing the nitro-coupling reactions.[38] In this case, the molecular oxygen could be considered as a charge carrier-relaying co-catalyst triggering the multistep reductive coupling reactions. As shown by our previous work,[38] pNTP chemisorbed on Ag nanoparticle surfaces remained unreactive without any observable level of DMAB formation when illuminated by a 785 nm excitation laser in an anaerobic reaction environment. The chemisorption of pNPA to Ag resulted in energy upshifts of the frontier orbitals of the adsorbates, and the calculated LUMO energy of pNPA-Ag_4 was 2.8 eV above the Ag Fermi level (Figure S5 in the Supporting Information). Therefore, even at the λ_{ex} of 532 nm, the hot electrons were energetically insufficient to get injected into the LUMO of chemisorbed pNPA. The pNPA coupling reactions could occur only through the O_2-mediated pathway at both excitation wavelengths. Our time-resolved SERS results revealed that the electron transfer from Ag to nitrophenyl adsorbates under visible light illumination was a kinetically more efficient reaction pathway in comparison to the O_2-mediated pathway under near-infrared excitations. Second, pNPA was observed to be substantially less reactive than pNTP under identical reaction conditions, suggesting that the π-back donation bonding mode reduced the reactivity of the nitrophenyl derivative adsorbates. The formation of the azo products required specific orientational arrangements of nitrophenyl adsorbates on the Ag nanoparticle surfaces.[30, 42, 43] Therefore, the orientations and structural flexibility, both of which were directly related to the bonding nature of the metal-adsorbate interactions, became critical factors modulating the reactivity of molecular adsorbates. We recently found that the π-back donation effect in Ag-ethynyl interactions made *para*-ethynylaniline adsorbates more tilted toward the Ag surface with significantly reduced structural flexibility, which led to declined reactivity toward oxidative coupling reactions.[55] The SERS results shown in Figure 2 revealed that the same rule could also be applied to the reductive coupling of chemisorbed nitrophenyl derivatives. Third, at λ_{ex} of 532 nm, pNTP appeared more reactive in an acidic environment than in an alkaline environment (Figure 2A) because this reductive coupling reaction involved protons.[39] However, elevated reactivity of chemisorbed pNPA was observed at λ_{ex} of 532 nm when switching from an acidic to an alkaline environment (Figure 2B), indicating that the effects of metal-adsorbate interactions should also be taken into consideration when interpreting the pH-dependence of the molecular reactivity. After taking a closer look at the detailed spectral lineshapes of the $\nu_{C\equiv C}$ mode in the wavenumber range of 1930-2060 cm^{-1} (Figure S6 in the Supporting Information), we found that the asymmetrically broaden spectral features could be deconvoluted into at least three peaks centered at 1960, 1990, and 2025 cm^{-1}, corresponding to three subpopulations labeled as I, II, and III, respectively. Higher degree of π-back donation in the Ag-ethynyl interactions led to larger spectral downshift of the $\nu_{C\equiv C}$ mode in the SERS spectra. The degree of π-back donation was highly likely to be related to the local surface curvature of Ag nanoparticles, which varied significantly from site to site. The chemisorbed pNPA with the lowest degree of π-back donation (subpopulation III) appeared to be the most reactive subpopulation, whereas the other two subpopulations remained drastically less reactive, further verifying the negative correlation between π-back donation and molecular reactivity. Within the time-duration of our SERS measurements, only a fraction of the chemisorbed pNPA was converted into DYAB. As the coupling reaction proceeded, the fraction of subpopulation III gradually decreased, while the spectral feature of the subpopulation I became increasingly more pronounced, indicating that the coupling of pNPA in the subpopulation III resulted in augmented π-back donation effect in the Ag-ethynyl interactions.

Through time-resolved SERS measurements, we systematically studied the kinetics of pNTP and pNPA coupling reactions in acidic (pH = 2) and alkaline (pH = 12) aqueous environments under continuous illumination by 532 nm and 758 nm lasers at various P_{ex}s. The reaction progress was tracked in real time based on the temporal evolution of Q, which was defined as the relative intensity of the ν_{NN} mode (at 1438 cm^{-1} for DMAB and 1448 cm^{-1} for DYAB, respectively) with respect to the $\nu_{CC\ ring}$ mode in the SERS spectra:

$$Q \equiv \frac{I(v_{NN})}{I(v_{CC\ ring})} \qquad \text{(Equation 1).}$$

In our case, the as-defined Q served as a descriptor of the apparent fractions of DMAB and DYAB during the pNTP and pNPA coupling reactions, respectively. Under each specific reaction condition, the SERS-based kinetic measurements were repeated at 5 different spots on the Ag nanoparticle arrays. Detailed kinetic results, including the temporally evolving Q trajectories collected from individual spots on the samples, the ensemble-averaged Q trajectories ($<Q>$) under each reaction condition, and the least squares curve-fitting results, are shown in Figures S7-S14 in the Supporting Information. In all cases, the kinetics of the bimolecular coupling reactions could be well-described by the following second-order rate law:

$$Q = \frac{2Q_{max}^2 k_{obs} t}{2Q_{max} k_{obs} t + 1} \qquad \text{(Equation 2)},$$

in which t is the reaction time, k_{obs} is the apparent second-order rate constant, and Q_{max} is the maximal Q achievable when t approaches infinity. The values of Q_{max} and k_{obs} under various reaction conditions were obtained by fitting the temporally evolving $<Q>$ trajectories with Equation 2.

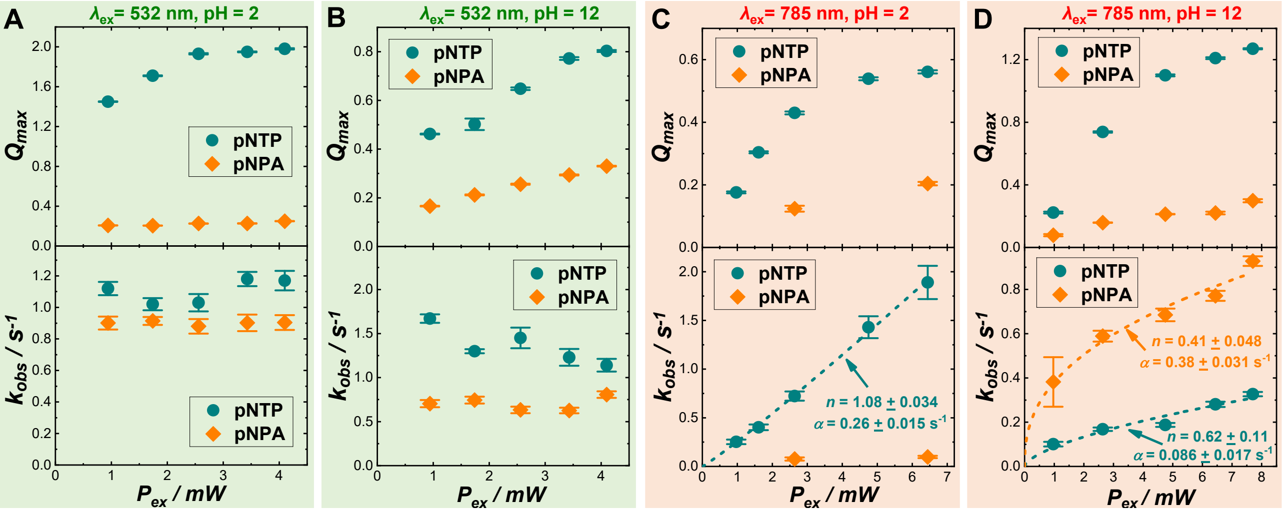

Figure 3. P_{ex}-dependence of (upper panel) Q_{max} and (lower panel) k_{obs} for the coupling reactions of pNTP and pNPA under 532 nm laser illumination at pHs of (A) 2 and (B) 12 and under 785 nm laser illumination at pHs of (C) 2 and (D) 12. The experimental results shown in the lower panels of C and D were fitted with Equation 3 and the fitting results are shown as dash curves.

Figure 3 shows the P_{ex}-dependent Q_{max} and k_{obs} of the pNTP and pNPA coupling reactions under various reaction conditions. At the λ_{ex} of 532 nm, Q_{max} increased monotonically as P_{ex} increased in both acidic and alkaline aqueous reaction media (upper panels in Figure 3A and 3B). Previous studies revealed that chemisorbed pNTP molecules could be activated for the reductive coupling reactions only when the local field intensities at the adsorbate-occupying sites exceeded a certain threshold value.[38] Increasing P_{ex} led to larger Q_{max} values as higher fractions of the pNTP adsorbates started to experience the local-field intensities above the threshold value. Such P_{ex} thresholds have also been previously observed on other plasmon-driven photoreactions, such as the oxidative coupling of aniline derivatives[55, 73, 74] and the decarboxylation of mercaptobenzobate.[75] The characteristic threshold P_{ex} values for different reactions varied significantly and were intimately tied to the chemical nature of the reactions, the excitation wavelengths, the local-field enhancements, and the local reaction environments. In contrast to the P_{ex}-dependence of Q_{max}, k_{obs} appeared almost independent of P_{ex} in both acidic and alkaline environments when P_{ex} was varied in the range of 1-5 mW (lower panels in Figure 3A and 3B). Although the coupling reactions were initiated by injection of hot electrons into the chemisorbed pNTP at the λ_{ex} of 532 nm, the apparent second-order kinetic features and P_{ex}-independent k_{obs} values strongly suggested that the rate-limiting step was associated with the bimolecular coupling of photo-activated adsorbates on the Ag surfaces under thermal conditions. Under continuous illumination by the 532 nm laser, pNTP was considerably more reactive than pNPA toward the coupling reactions, as evidenced by the fact that both the Q_{max} *and* k_{obs} of the pNTP coupling reactions exhibited higher values than those of the pNPA coupling reactions under each specific reaction condition. When switching the λ_{ex} from 532 nm to 785 nm, a similar P_{ex}-dependence of Q_{max} (Q_{max} increased with P_{ex}) was observed on both pNTP and pNPA coupling reactions, except that the Q_{max} values at λ_{ex} of 785 nm were significantly lower than those at λ_{ex} of 532 nm (upper panels in Figure 3C and 3D). The P_{ex}-dependence of k_{obs} at λ_{ex} of 785 nm (lower panels in

Figure 3C and 3D) became substantially different from that at λ_{ex} of 532 nm. We fitted the P_{ex}-dependence of k_{obs} with the following power function:

$$k_{obs} = \alpha \left(\frac{P_{ex}}{1\ mW}\right)^{n} \qquad \text{(Equation 3),}$$

in which n is an exponent and α is a fractional coefficient. As shown in the lower panel of Figure 3C, the n value obtained from curve fitting for the pNTP coupling reactions at λ_{ex} of 785 nm and pH of 2 was very close to 1. Although k_{obs} appeared to be linearly proportional to P_{ex} for the pNTP coupling reactions, pNPA showed limited reactivity featured by much smaller Q_{max} and k_{obs} values within the same P_{ex} range. The origin of the linear power dependence of k_{obs} observed on the pNTP coupling reactions could be well-interpreted in the context of the O_2-mediated reaction mechanism. At λ_{ex} of 785 nm, the plasmonic hot electrons were injected into the π* orbital of surface-adsorbed O_2 instead of the LUMO of surface-adsorbed pNTP. As shown in detail by our previous work,[74] the overall reaction kinetics were essentially modulated by the photoactivated O_2^- radicals at its steady state concentrations, which exhibited a linear dependence on P_{ex}. The linear P_{ex}-dependence of k_{obs} also indicated that under this reaction condition, the pNTP coupling reaction was driven by plasmonic hot electrons without any significant influence by photothermal heating.[9, 15, 76] Because of the small excitation volume of the confocal illumination and high thermal conductivity of water, the heat produced through photothermal transduction was rapidly dissipated to the aqueous reaction environment, resulting in rather insignificant elevation of the local temperatures on the photocatalyst surfaces.[75, 77] In alkaline environments, 785 nm excitations gave rise to sublinear P_{ex}-dependence of k_{obs} for both pNTP and pNPA coupling reactions (lower panel of Figure 3D). Such sublinearity in power dependence is a common feature of semiconductor-driven photocatalytic reactions when the bulk electron-hole pair recombination becomes prevalent but has been rarely observed in plasmon-driven photocatalysis on metallic nanostructures.[9] The plasmon-driven reductive coupling of nitrophenyl derivatives under near-infrared excitations involves not only the photoactivated O_2^- but also protons. We hypothesized that the limited availability of protons in an alkaline reaction environment might become a kinetic bottleneck in the high P_{ex} regime. The detailed mechanisms underpinning the sublinear power-dependence of k_{obs}, however, still need to be further investigated. Although higher k_{obs} values were observed on pNPA than on pNTP at same P_{ex}s (lower panel of Figure 3D), the Q_{max} values of the pNPA coupling reactions were substantially lower than those of the pNTP coupling reactions (upper panel of Figure 3D), suggesting that only a small fraction of surface-adsorbed pNPA, probably the above-mentioned subpopulation III, remained reactive in an alkaline environment at λ_{ex} of 785 nm.

The covalent interactions between the isocyano group of pNPI and the Ag nanoparticle surfaces were chemically more versatile than the Ag-thiol and Ag-ethynyl interactions. We found that pNPI molecules were chemisorbed to Ag surfaces through unique pH-dependent bimodal interactions, which were σ-bonding in nature in an acidic environment but became dominated by π-back donation in an alkaline environment. As shown in Figure 4A, the Raman shifts of various major vibrational modes, including the $\nu_{\mathrm{CC\ ring}}$, ν_{NO2}, β_{NO2}, and β_{CH} modes, in the SERS spectra of chemisorbed pNPI at pH of 2 matched those in the normal Raman spectrum of neat pNPI, except for the peak position of the stretching mode of N≡C bond (ν_{NC}). The ν_{NC} mode was upshifted from 2130 cm^{-1} in the normal Raman spectrum to 2186 cm^{-1} in the SERS spectrum collected at pH of 2 due to σ-donation of electrons from Ag to the isocyano group. In contrast, at pH of 12, the ν_{NC} mode in the SERS spectrum was downshifted to 1974 cm^{-1} and became significantly weakened and broadened due to π-back donation of electrons from the valence band of Ag to the antibonding π* orbital of the isocyano group. Through DFT calculations, we identified two optimized structures of the pNPI-Ag$_4$ complex, denoted as pNPI-Ag$_4$-i and pNPI-Ag$_4$-ii, respectively. pNPI-Ag$_4$-i adopted an atop conformation with the C atom in the isocyano group forming a covalent σ-bond with an Ag atom (Figure 4B). The σ-donation of electrons from Ag to the isocyano group led to shortening of the N≡C bond. The upshift of the ν_{NC} mode in SERS with respect to that in the normal Raman spectra signified the σ-donation mode of the

Ag-isocyano interactions, as exemplified not only by the chemisorbed pNPI studied in this work but also by other previously investigated isocyanyl derivatives, such as 2,6-dimethylphenyl isocyanide and 1,4-phenylene diisocyanide.[67-69] In contrast, pNPI-Ag_4-ii adopted a bridge conformation with the C atom interacting with two Ag atoms simultaneously (Figure 4C). The LUMO energies of pNPI-Ag_4-i and pNPI-Ag_4-ii were calculated to be 1.1 and 1.4 eV above the Ag Fermi level, respectively (Figure S15 in the Supporting Information). When adopting the bridge conformation, the chemisorbed pNPI molecule was more tilted toward the Ag surfaces, which enabled the π* orbital of N≡C to overlap with the valence orbital of Ag. Such bridge conformation also allowed the nitro group of pNPI to develop non-covalent interactions with the Ag surfaces, which was reflected by the spectral downshift and asymmetric lineshape broadening of both the ν_{NO2} and β_{NO2} modes in the SERS spectrum of pNPI at the pH of 12 (Figure 4A). All the experimentally observed pH-dependent SERS spectral features, including the upshift of the ν_{NC} mode caused by σ-donation and the downshifts of the ν_{NC}, ν_{NO2} and β_{NO2} modes caused by π-back donation, were also fully captured by the DFT-calculated Raman spectra shown in Figure 4D.

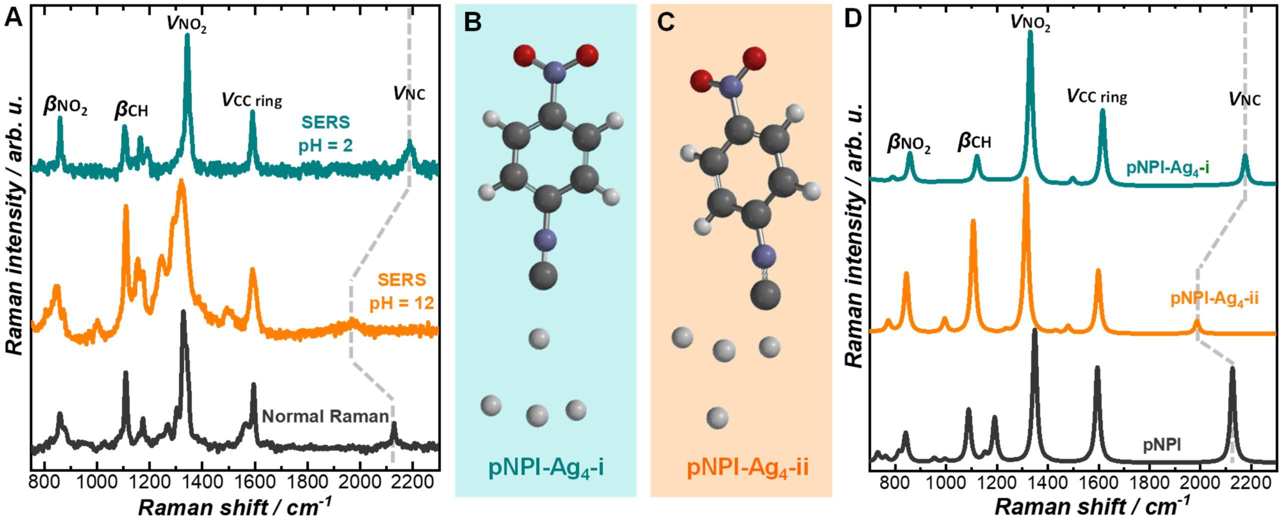

Figure 4. (A) Experimentally measured normal Raman spectrum of pNPI and SERS spectra of pNPI chemisorbed to Ag nanoparticle surfaces at pHs of 2 and 12. The normal Raman spectrum was collected from a solid sample of neat pNPI at a λ_{ex} of 785 nm and a P_{ex} of 6.44 mW with a spectral integration time of 20 s. The SERS spectra were collected at a λ_{ex} of 785 nm and a P_{ex} of 0.29 mW with a spectral integration time of 5 s. The assignments of several major Raman peaks are labeled.

Molecular structures optimized by DFT for (B) pNPI-Ag_4-i and (C) pNPI-Ag_4-ii. (D) DFT-calculated Raman spectra of pNPI, pNPI-Ag_4-i, and pNPI-Ag_4-ii.

The different bonding nature of the Ag-isocyano interactions resulted in remarkably different levels of adsorbate reactivity in acidic and alkaline environments. When switching the pH of the reaction medium from 2 to 12, the chemisorbed pNPI molecules became substantially less reactive at λ_{ex}s of both 532 and 785 nm as the π-back donation effect started to dominate the metal-adsorbate interactions. As the pNPI coupling reaction proceeded, the signature SERS peaks of *p,p′*-diisocyanoazobenzene (DIAB), including the ν_{CN} mode at 1140 cm^{-1} and the ν_{NN} modes at 1456 and 1406 cm^{-1}, emerged and became increasingly more pronounced, while the ν_{NO2} mode at 1342 cm^{-1}, the β_{NO2} mode at 860 cm^{-1}, and the β_{CH} mode of pNPI at 1107 cm^{-1} all became progressively weaker in the time-resolved SERS spectra (Figure 5A and 5B). After comparing the experimentally resolved spectral features to the DFT results (Figure S16 in Supporting Information), we concluded that the as-produced DIAB molecules were in the *trans*- rather than the *cis*-conformation, analogous to the DMAB and DYAB molecules produced through the plasmon-driven coupling reactions. In an acidic environment, both the peak position and the spectral lineshape of the ν_{NC} mode remained essentially unchanged during the coupling reactions (Figure S17 in Supporting Information), indicating that the resulting DIAB molecules were also chemisorbed to Ag surfaces through σ-donation. We systematically compared the plasmonic reactivity and the coupling rates of pNPI on Ag nanoparticle arrays at pHs of 2 and 12 under continuous illuminations by the 532 nm and 785 nm lasers at different P_{ex}s. The detailed kinetic results are shown in Figures S18-21 in the Supporting Information. At the λ_{ex} of 532 nm, the pNPI coupling reactions at the pH of 2 were kinetically so fast that Q reached its maximal values within one frame of the time-resolved SERS measurements. Therefore, the detailed reaction kinetics became irresolvable with the current time-resolution of our SERS measurements (300 ms). At the λ_{ex} of 532 nm, the Q_{max} values associated with the pNPI coupling reactions at the pH of 2 remained around 0.37, almost independent of P_{ex} (Figure 5C). Such P_{ex}-independent Q_{max} indicated that the P_{ex}-threshold for photoactivation of chemisorbed pNPI was significantly lower than those of pNTP and pNPA, and all the reactive subpopulations of pNPI adsorbates were rapidly converted into DIAB in the P_{ex} range we investigated. At the λ_{ex} of 785 nm and the pH of 2, the Q_{max} values also appeared P_{ex}-dependent (Figure 5D), whereas the kinetics of the pNPI coupling reactions became clearly resolvable by our SERS measurements. A nearly linear relationship between k_{obs} and P_{ex} was observed when P_{ex} was varied in the range of 1-5 mW (Figure 5E). At the pH of 12, however, the coupling reactions became kinetically sluggish with very limited yields of DIAB achieved within the time-durations of our SERS measurements (Figure 5C and 5D). The SERS results on the pNPI coupling reactions clearly showed that the π-back donation in Ag-isocyano interactions led to significantly decreased plasmonic reactivity of chemisorbed pNPI toward the reductive coupling reactions, fully in line with our observations on the pNTP and pNPA coupling reactions.

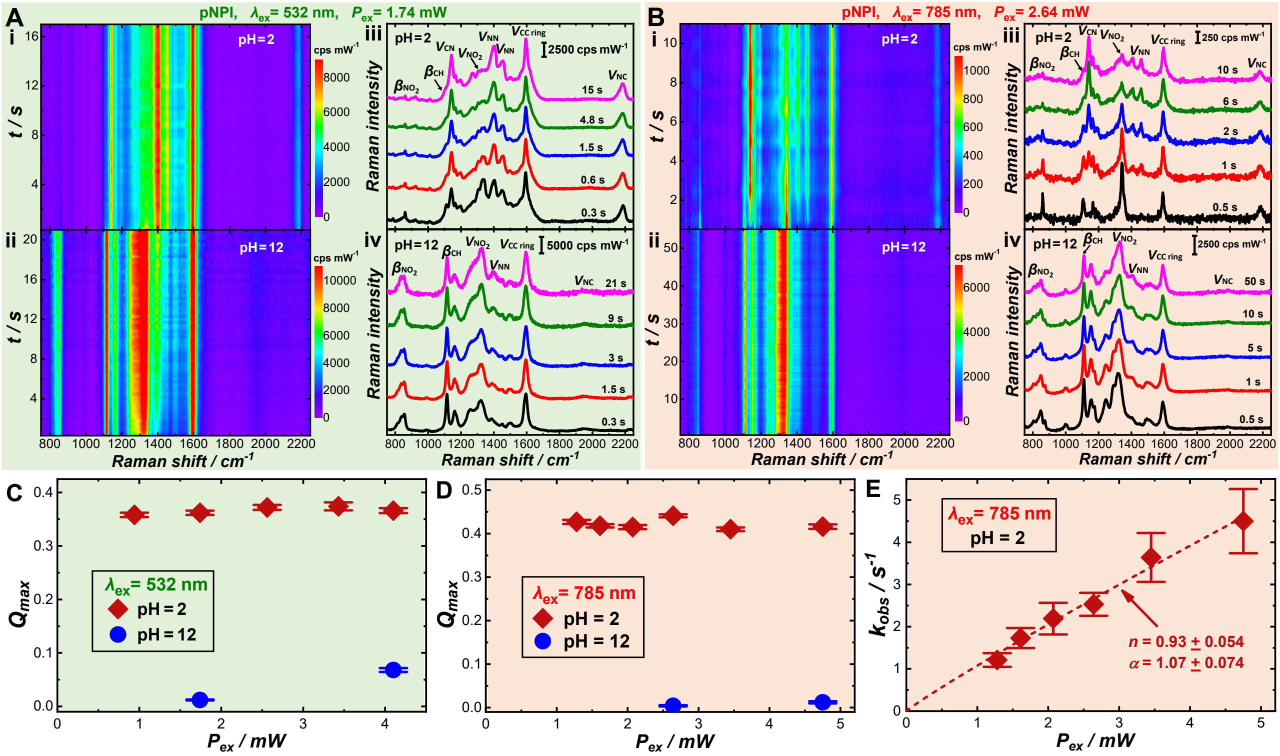

Figure 5. Time-resolved SERS spectra at pHs of (i) 2 and (ii) 12 and snap-shot SERS spectra captured at various reaction times at pHs of (iii) 2 and (iv) 12 during plasmon-driven pNPI coupling reactions at (A) λ_{ex} of 532 nm and P_{ex} of 1.74 mW and (B) λ_{ex} of 785 nm and P_{ex} of 2.64 mW. P_{ex}-dependence

of Q_{max} for pNPI coupling reactions under (C) 532 nm and (D) 785 nm laser excitations at pHs of 2 and 12. (E) P_{ex}-dependence of k_{obs} for pNPI coupling reactions at λ_{ex} of 785 nm and pH of 2. The experimental results were fitted with Equation 3 and the fitting results are shown as the dash curve in panel E.

CONCLUSIONS

Using SERS as an *in situ* molecular fingerprinting tool, we have been able to correlate the molecule-transforming kinetics to detailed adsorbate structures during plasmon-driven reductive coupling of nitrophenyl derivatives chemisorbed to Ag nanoparticle surfaces. In our systematic comparative studies, pNTP, pNPA, and pNPI are selected as three representative nitrophenyl derivatives that utilize fundamentally distinct functional groups as the surface-anchoring moieties to form covalent interactions with metallic Ag. A chemisorbed pNTP molecule uses its thiol group to interact with metallic Ag through an Ag-S σ bond, whereas the interactions between the ethynyl group in pNPA and the Ag nanoparticle surfaces are dominated by π-back donation. In comparison to the Ag-thiol and Ag-ethynyl interactions, the bonding nature of the interactions between the isocyano group in pNPI and metallic Ag is chemically more versatile, exhibiting the characteristics of σ-donation in an acidic environment but switching to the π-back donation mode in an alkaline environment. The differences in the chemical nature of metal-adsorbate interactions lead to remarkably different levels of plasmonic reactivity among the three nitrophenyl derivatives investigated in this work. The pathways of hot electron transfer can be fundamentally altered and the detailed kinetic features of the coupling reactions (the apparent rate constants, the maximal reaction yields, and the excitation power dependence) can be significantly modified upon variation of either the excitation wavelength or the pH in the aqueous reaction medium. In spite of the mechanistic complexity and versatility, we have consistently observed that the σ-bonding mode in the metal-adsorbate interactions favors the plasmon-driven reductive coupling reactions, whereas the π-back donation effect leads to significant decrease in the plasmonic reactivity of the nitrophenyl derivative adsorbates. The origin of different plasmonic reactivity observed among various nitrophenyl derivative adsorbates can be interpreted in the context of several interesting effects associated with the chemical nature of metal-adsorbate interactions. First, switching the chemisorption mode from σ-donation to π-back donation results in significantly altered surface orientations of the chemisorbed nitrophenyl derivatives, making the molecular conformations less favorable for the plasmon-driven bimolecular coupling reactions. Second, the structural flexibility of the nitrophenyl derivative adsorbates is reduced as the molecular adsorbates are oriented in closer contact with the metal surfaces when the metal-adsorbate interactions become dominated by π-back donation. Such reduced structural flexibility restricts the conformational changes of the molecular adsorbates during the coupling reactions. Third, the chemical nature of the metal-adsorbate interactions may also influence the LUMO energies of the molecular adsorbates. Our DFT calculations indicate that the π-back donation effects may cause energy upshifts of the LUMOs of nitrophenyl derivative adsorbates on Ag surfaces, raising the energy barriers for metal-to-adsorbate transfer of plasmonic hot electrons. The key findings reported in this work clearly indicate that the plasmonic reactivity and transforming kinetics of molecular adsorbates are not only related to the plasmonic properties of the nanostructured metallic adsorbents, but also rigorously dictated by the bonding nature of the metal-adsorbate interactions.

ASSOCIATED CONTENT

Supporting Information. Protocol for nanoparticle synthesis, instruments used for nanostructure characterizations, details of DFT calculations, and additional figures as noted in the maintext, including TEM image, size distribution, and optical extinction spectrum of Ag nanoparticles, calculated frontier orbital energies of molecular adsorbates, SERS spectra of various nitrophenyl derivative adsorbates, detailed kinetic results under various reaction conditions, and DFT-calculated Raman spectra of aromatic azo compounds. This material is available free of charge via the Internet at http://pubs.acs.org.

AUTHOR INFORMATION

Corresponding Author

* Hui Wang − Department of Chemistry and Biochemistry, University of South Carolina, Columbia, South Carolina 29208; Email: *wang344@mailbox.sc.edu*; Phone: 1-803-777-2203; orcid.org/0000-0002-1874-5137.

Author

Kexun Chen − Department of Chemistry and Biochemistry, University of South Carolina, Columbia, South Carolina 29208; orcid.org/0000-0003-2809-1242.

Author Contributions

K.C. did all the experimental and computational work. K.C and H.W. analyzed the data. H.W. designed the project, supervised the research, acquired funding support, and wrote the paper. Both authors have given approval to the final version of the manuscript.

Notes

The authors declare no competing financial interest.

ACKNOWLEDGMENT

This work was supported by the Macromolecular, Supramolecular, and Nanochemistry (MSN) Program in the Division of Chemistry of the National Science Foundation (NSF) under Grant CHE-2202928. K.C. was partially supported by a SPARC Award (130200-22-59284) sponsored by the University of South Carolina Office of Vice President for Research. The Zeiss Gemini500 thermal field emission scanning electron microscope used in this work was purchased using the South Carolina Science, Technology, Engineering, and Mathematics (STEM) Equipment Funds. The Hitachi HT7800 transmission electron microscope used in this work was purchased using funds provided by an NSF EPSCoR RII Track-I Award (OIA-1655740).

REFERENCES

1. Kazuma, E.; Kim, Y. Mechanistic Studies of Plasmon Chemistry on Metal Catalysts. *Angew. Chem. Inter. Ed.* **2019,** *58* (15), 4800-4808.
2. Gelle, A.; Jin, T.; de la Garza, L.; Price, G. D.; Besteiro, L. V.; Moores, A. Applications of Plasmon-Enhanced Nanocatalysis to Organic Transformations. *Chem. Rev.* **2020,** *120* (2), 986-1041.
3. Christopher, P.; Moskovits, M. Hot Charge Carrier Transmission from Plasmonic Nanostructures. *Annu. Rev. Phys. Chem.* **2017,** *68*, 379-398.
4. Park, J. Y.; Kim, S. M.; Lee, H.; Nedrygailov, I. I. Hot-Electron-Mediated Surface Chemistry: Toward Electronic Control of Catalytic Activity. *Acc. Chem. Res.* **2015,** *48* (8), 2475-2483.
5. Brongersma, M. L.; Halas, N. J.; Nordlander, P. Plasmon-Induced Hot Carrier Science and Technology. *Nat. Nanotech.* **2015,** *10* (1), 25-34.

6. Zhang, Y. C.; He, S.; Guo, W. X.; Hu, Y.; Huang, J. W.; Mulcahy, J. R.; Wei, W. D. Surface-Plasmon-Driven Hot Electron Photochemistry. *Chem. Rev.* **2018,** *118* (6), 2927-2954.

7. Zhang, Z. L.; Zhang, C. Y.; Zheng, H. R.; Xu, H. X. Plasmon-Driven Catalysis on Molecules and Nanomaterials. *Acc. Chem. Res.* **2019,** *52* (9), 2506-2515.

8. Tang, H. B.; Chen, C. J.; Huang, Z. L.; Bright, J.; Meng, G. W.; Liu, R. S.; Wu, N. Q. Plasmonic Hot Electrons for Sensing, Photodetection, and Solar Energy Applications: A Perspective. *J. Chem. Phys.* **2020,** *152* (22), 220901.

9. Kale, M. J.; Avanesian, T.; Christopher, P. Direct Photocatalysis by Plasmonic Nanostructures. *ACS Catal.* **2014,** *4* (1), 116-128.

10. Linic, S.; Aslam, U.; Boerigter, C.; Morabito, M. Photochemical Transformations on Plasmonic Metal Nanoparticles. *Nat. Mater.* **2015,** *14* (6), 567-576.

11. Linic, S.; Christopher, P.; Ingram, D. B. Plasmonic-Metal Nanostructures for Efficient Conversion of Solar to Chemical Energy. *Nat. Mater.* **2011,** *10* (12), 911-921.

12. Kherbouche, I.; Luo, Y.; Felidj, N.; Mangeney, C. Plasmon-Mediated Surface Functionalization: New Horizons for the Control of Surface Chemistry on the Nanoscale. *Chem. Mater.* **2020,** *32* (13), 5442-5454.

13. Devasia, D.; Das, A.; Mohan, V.; Jain, P. K. Control of Chemical Reaction Pathways by Light-Matter Coupling. *Annu. Rev. Phys. Chem.* **2021,** *72*, 423-443.

14. Li, S. S.; Huang, H.; Shao, L.; Wang, J. F. How to Utilize Excited Plasmon Energy Efficiently. *ACS Nano* **2021,** *15* (7), 10759-10768.

15. Cortés, E.; Besteiro, L. V.; Alabastri, A.; Baldi, A.; Tagliabue, G.; Demetriadou, A.; Narang, P. Challenges in Plasmonic Catalysis. *ACS Nano* **2020,** *14* (12), 16202-16219.

16. Li, J. T.; Cushing, S. K.; Meng, F. K.; Senty, T. R.; Bristow, A. D.; Wu, N. Q. Plasmon-Induced Resonance Energy Transfer for Solar Energy Conversion. *Nat. Photon.* **2015,** *9* (9), 601-607.

17. Govorov, A. O.; Zhang, H.; Demir, H. V.; Gun'ko, Y. K. Photogeneration of Hot Plasmonic Electrons with Metal Nanocrystals: Quantum Description and Potential Applications. *Nano Today* **2014,** *9* (1), 85-101.

18. van Schrojenstein Lantman, E. M.; Deckert-Gaudig, T.; Mank, A. J. G.; Deckert, V.; Weckhuysen, B. M. Catalytic Processes Monitored at the Nanoscale with Tip-Enhanced Raman Spectroscopy. *Nat. Nanotech.* **2012,** *7* (9), 583-586.

19. Zhan, C.; Chen, X. J.; Huang, Y. F.; Wu, D. Y.; Tian, Z. Q. Plasmon-Mediated Chemical Reactions on Nanostructures Unveiled by Surface-Enhanced Raman Spectroscopy. *Acc. Chem. Res.* **2019,** *52* (10), 2784-2792.

20. Sun, M. T.; Xu, H. X. A Novel Application of Plasmonics: Plasmon-Driven Surface-Catalyzed Reactions. *Small* **2012,** *8* (18), 2777-2786.

21. Chen, K. X.; Wang, H. Plasmon-Driven Photocatalytic Molecular Transformations on Metallic Nanostructure Surfaces: Mechanistic Insights Gained from Plasmon-Enhanced Raman Spectroscopy. *Mole. Syst. Des. Eng.* **2021,** *6* (4), 250-280.

22. Schlucker, S. Surface-Enhanced Raman Spectroscopy: Concepts and Chemical Applications. *Angew. Chem. Inter. Ed.* **2014,** *53* (19), 4756-4795.

23. Chen, X. J.; Cabello, G.; Wu, D. Y.; Tian, Z. Q. Surface-Enhanced Raman Spectroscopy toward Application in Plasmonic Photocatalysis on Metal Nanostructures. *J. Photochem. Photobiol. C-Photochem. Rev.* **2014,** *21*, 54-80.

24. Rizevsky, S.; Kurouski, D. Tip-Enhanced Raman Imaging of Photocatalytic Processes at the Nanoscale. *J. Phys. Chem. C* **2022,** *126* (35), 14781-14790.

25. Li, Z. D.; Kurouski, D. Plasmon-Driven Chemistry on Mono- and Bimetallic Nanostructures. *Acc. Chem. Res.* **2021,** *54* (10), 2477-2487.

26. Xie, W.; Schlucker, S. Hot Electron-Induced Reduction of Small Molecules on Photorecycling Metal Surfaces. *Nat. Commun.* **2015,** *6,* 7570.

27. Brooks, J. L.; Frontiera, R. R. Competition between Reaction and Degradation Pathways in Plasmon-Driven Photochemistry. *J. Phys. Chem. C* **2016,** *120* (37), 20869-20876.

28. Golubev, A. A.; Khlebtsov, B. N.; Rodriguez, R. D.; Chen, Y.; Zahn, D. R. T. Plasmonic Heating Plays a Dominant Role in the Plasmon-Induced Photocatalytic Reduction of 4-Nitrobenzenethiol. *J. Phys. Chem. C* **2018,** *122* (10), 5657-5663.

29. Wang, C. F.; O'Callahan, B. T.; Kurouski, D.; Krayev, A.; El-Khoury, P. Z. The Prevalence of Anions at Plasmonic Nanojunctions: A Closer Look at p-Nitrothiophenol. *J. Phys. Chem. Lett.* **2020,** *11* (10), 3809-3814.

30. Sun, J. J.; Su, H. S.; Yue, H. L.; Huang, S. C.; Huang, T. X.; Hu, S.; Sartin, M. M.; Cheng, J.; Ren, B. Role of Adsorption Orientation in Surface Plasmon-Driven Coupling Reactions Studied by Tip-Enhanced Raman Spectroscopy. *J. Phys. Chem. Lett.* **2019,** *10* (10), 2306-2312.

31. Kang, L. L.; Xu, P.; Zhang, B.; Tsai, H. H.; Han, X. J.; Wang, H. L. Laser Wavelength- and Power-Dependent Plasmon-Driven Chemical Reactions Monitored Using Single Particle Surface Enhanced Raman Spectroscopy. *Chem. Commun.* **2013,** *49* (33), 3389-3391.

32. Kang, L. L.; Han, X. J.; Chu, J. Y.; Xiong, J.; He, X.; Wang, H. L.; Xu, P. In Situ Surface-Enhanced Raman Spectroscopy Study of Plasmon-Driven Catalytic Reactions of 4-Nitrothiophenol under a Controlled Atmosphere. *ChemCatChem* **2015,** *7* (6), 1004-1010.

33. Choi, H. K.; Lee, K. S.; Shin, H. H.; Kim, Z. H. Identification of the First Elementary Step in the Photocatalytic Reduction of Nitrobenzenethiols on a Metallic Surface. *J. Phys. Chem. Lett.* **2016,** *7* (20), 4099-4104.

34. Koopman, W.; Sarhan, R. M.; Stete, F.; Schmitt, C. N. Z.; Bargheer, M. Decoding the Kinetic Limitations of Plasmon Catalysis: The Case of 4-Nitrothiophenol Dimerization. *Nanoscale* **2020,** *12* (48), 24411-24418.

35. Dong, B.; Fang, Y. R.; Xia, L. X.; Xu, H. X.; Sun, M. T. Is 4-Nitrobenzenethiol Converted to p,p'-Dimercaptoazobenzene or 4-Aminothiophenol by Surface Photochemistry Reaction? *J. Raman Spectrosc.* **2011,** *42* (6), 1205-1206.

36. Miao, P.; Ma, Y.; Sun, M. T.; Li, J.; Xu, P. Tuning the Sers Activity and Plasmon-Driven Reduction of p-Nitrothiophenol on a Ag@MoS_2 Film. *Faraday Discussions* **2019,** *214*, 297-307.

37. Sarhan, R. M.; Koopman, W.; Schuetz, R.; Schmid, T.; Liebig, F.; Koetz, J.; Bargheer, M. The Importance of Plasmonic Heating for the Plasmon-Driven Photodimerization of 4-Nitrothiophenol. *Sci. Rep.* **2019,** *9*, 3060.

38. Zhang, Q. F.; Zhou, Y. D.; Fu, X. Q.; Villarreal, E.; Sun, L. C.; Zou, S. L.; Wang, H. Photothermal Effect, Local Field Dependence, and Charge Carrier Relaying Species in Plasmon-Driven Photocatalysis: A Case Study of Aerobic Nitrothiophenol Coupling Reaction. *J. Phys. Chem. C* **2019,** *123* (43), 26695-26704.

39. Dong, B.; Fang, Y. R.; Chen, X. W.; Xu, H. X.; Sun, M. T. Substrate-, Wavelength-, and Time-Dependent Plasmon-Assisted Surface Catalysis Reaction of 4-Nitrobenzenethiol Dimerizing to P,P '-Dimercaptoazobenzene on Au, Ag, and Cu Films. *Langmuir* **2011,** *27* (17), 10677-10682.

40. Choi, H. K.; Park, W. H.; Park, C. G.; Shin, H. H.; Lee, K. S.; Kim, Z. H. Metal-Catalyzed Chemical Reaction of Single Molecules Directly Probed by Vibrational Spectroscopy. *J. Am. Chem. Soc.* **2016,** *138* (13), 4673-4684.

41. Keller, E. L.; Frontiera, R. R. Ultrafast Nanoscale Raman Thermometry Proves Heating Is Not a Primary Mechanism for Plasmon-Driven Photocatalysis. *ACS Nano* **2018,** *12* (6), 5848-5855.

42. Cai, Z. F.; Merino, J. P.; Fang, W.; Kumar, N.; Richardson, J. O.; De Feyter, S.; Zenobi, R. Molecular-Level Insights on Reactive Arrangement in on-Surface Photocatalytic Coupling Reactions Using Tip-Enhanced Raman Spectroscopy. *J. Am. Chem. Soc.* **2022,** *144* (1), 538-546.

43. Koopman, W.; Titov, E.; Sarhan, R. M.; Gaebel, T.; Schurmann, R.; Mostafa, A.; Kogikoski, S.; Stete, F.; Liebig, F.; Schmitt, C. N. Z.; Koetz, J.; Bald, I.; Saalfrank, P.; Bargheer,

M.; Milosavjevio, A. R. The Role of Structural Flexibility in Plasmon-Driven Coupling Reactions: Kinetic Limitations in the Dimerization of Nitro-Benzenes. *Adv. Mater. Interfaces* **2021,** *8* (22), 2101344.

44. Love, J. C.; Estroff, L. A.; Kriebel, J. K.; Nuzzo, R. G.; Whitesides, G. M. Self-Assembled Monolayers of Thiolates on Metals as a Form of Nanotechnology. *Chem. Rev.* **2005,** *105* (4), 1103-1169.

45. Pinson, J.; Podvorica, F. Attachment of Organic Layers to Conductive or Semiconductive Surfaces by Reduction of Diazonium Salts. *Chem. Soc. Rev.* **2005,** *34* (5), 429-439.

46. Cao, C.; Zhang, Y.; Jiang, C.; Qj, M.; Liu, G. Advances on Aryldiazonium Salt Chemistry Based Interfacial Fabrication for Sensing Applications. *ACS Appl. Mater. Interfaces* **2017,** *9* (6), 5031-5049.

47. Laurentius, L.; Stoyanov, S. R.; Gusarov, S.; Kovalenko, A.; Du, R. B.; Lopinski, G. P.; McDermott, M. T. Diazonium-Derived Aryl Films on Gold Nanoparticles: Evidence for a Carbon-Gold Covalent Bond. *ACS Nano* **2011,** *5* (5), 4219-4227.

48. Mesnage, A.; Lefevre, X.; Jegou, P.; Deniau, G.; Palacin, S. Spontaneous Grafting of Diazonium Salts: Chemical Mechanism on Metallic Surfaces. *Langmuir* **2012,** *28* (32), 11776-11787.

49. Ahmad, R.; Boubekeur-Lecaque, L.; Nguyen, M.; Lau-Truong, S.; Lamouri, A.; Decorse, P.; Galtayries, A.; Pinson, J.; Felidj, N.; Mangeney, C. Tailoring the Surface Chemistry of Gold Nanorods through Au-C/Ag-C Covalent Bonds Using Aryl Diazonium Salts. *J. Phys. Chem. C* **2014,** *118* (33), 19098-19105.

50. Han, X. M.; Lee, H. K.; Lee, Y. H.; Hao, W.; Liu, Y. J.; Phang, I. Y.; Li, S. Z.; Ling, X. Y. Identifying Enclosed Chemical Reaction and Dynamics at the Molecular Level Using Shell-Isolated Miniaturized Plasmonic Liquid Marble. *J. Phys. Chem. Lett.* **2016,** *7* (8), 1501-1506.

51. Fracasso, D.; Kumar, S.; Rudolf, P.; Chiechi, R. C. Self-Assembled Monolayers of Terminal Acetylenes as Replacements for Thiols in Bottom-up Tunneling Junctions. *RSC Adv.* **2014,** *4* (99), 56026-56030.

52. Feng, Y. H.; Xing, S. X.; Xu, J.; Wang, H.; Lim, J. W.; Chen, H. Y. Probing the Kinetics of Ligand Exchange on Colloidal Gold Nanoparticles by Surface-Enhanced Raman Scattering. *Dalton Transactions* **2010,** *39* (2), 349-351.

53. Feilchenfeld, H.; Weaver, M. J. Binding of Alkynes to Silver, Gold, and Underpotential-Deposited Silver Electrodes as Deduced by Surface-Enhanced Raman-Spectroscopy. *J. Phys. Chem.* **1989,** *93* (10), 4276-4282.

54. Maity, P.; Takano, S.; Yamazoe, S.; Wakabayashi, T.; Tsukuda, T. Binding Motif of Terminal Alkynes on Gold Clusters. *J. Am. Chem. Soc.* **2013,** *135* (25), 9450-9457.

55. Chen, K. X.; Wang, H. Plasmon-Driven Oxidative Coupling of Aniline-Derivative Adsorbates: A Comparative Study of Para-Ethynylaniline and Para-Mercaptoaniline. *J. Chem. Phys.* **2022,** *156* (20), 204705.

56. Yang, Y. Q.; Luo, J. B.; Song, P.; Ding, Y.; Xia, L. X. Novel Clarification of Surface Plasmon Coupling Reactions of Aromatic Alkynamine and Nitro Compounds. *ACS Omega* **2022,** *7* (1), 1165-1172.

57. Crudden, C. M.; Horton, J. H.; Ebralidze, I. I.; Zenkina, O. V.; McLean, A. B.; Drevniok, B.; She, Z.; Kraatz, H.-B.; Mosey, N. J.; Seki, T., et al. Ultra Stable Self-Assembled Monolayers of N-Heterocyclic Carbenes on Gold. *Nat. Chem.* **2014,** *6* (5), 409-414.

58. Hopkinson, M. N.; Richter, C.; Schedler, M.; Glorius, F. An Overview of N-Heterocyclic Carbenes. *Nature* **2014,** *510* (7506), 485-496.

59. Crudden, C. M.; Horton, J. H.; Narouz, M. R.; Li, Z.; Smith, C. A.; Munro, K.; Baddeley, C. J.; Larrea, C. R.; Drevniok, B.; Thanabalasingam, B., et al. Simple Direct Formation of Self-

Assembled N-Heterocyclic Carbene Monolayers on Gold and Their Application in Biosensing. *Nat. Commun.* **2016,** *7*, 12654.

60. Zhukhovitskiy, A. V.; Mavros, M. G.; Van Voorhis, T.; Johnson, J. A. Addressable Carbene Anchors for Gold Surfaces. *J. Am. Chem. Soc.* **2013,** *135* (20), 7418-7421.

61. DeJesus, J. F.; Trujillo, M. J.; Camden, J. P.; Jenkins, D. M. N-Heterocyclic Carbenes as a Robust Platform for Surface-Enhanced Raman Spectroscopy. *J. Am. Chem. Soc.* **2018,** *140* (4), 1247-1250.

62. Trujillo, M. J.; Strausser, S. L.; Becca, J. C.; DeJesus, J. F.; Jensen, L.; Jenkins, D. M.; Camden, J. P. Using Sers to Understand the Binding of N-Heterocyclic Carbenes to Gold Surfaces. *J. Phys. Chem. Lett.* **2018,** *9* (23), 6779-6785.

63. Swanson, S. A.; McClain, R.; Lovejoy, K. S.; Alamdari, N. B.; Hamilton, J. S.; Scott, J. C. Self-Assembled Diisocyanide Monolayer Films on Gold and Palladium. *Langmuir* **2005,** *21* (11), 5034-5039.

64. Stapleton, J. J.; Daniel, T. A.; Uppili, S.; Cabarcos, O. M.; Naciri, J.; Shashidhar, R.; Allara, D. L. Self-Assembly, Characterization, and Chemical Stability of Isocyanide-Bound Molecular Wire Monolayers on Gold and Palladium Surfaces. *Langmuir* **2005,** *21* (24), 11061-11070.

65. Joo, S. W.; Kim, W. J.; Yoon, W. S.; Choi, I. S. Adsorption of 4,4 '-Biphenyl Diisocyanide on Gold Nanoparticle Surfaces Investigated by Surface-Enhanced Raman Scattering. *J. Raman Spectrosc.* **2003,** *34* (4), 271-275.

66. Henderson, J. I.; Feng, S.; Ferrence, G. M.; Bein, T.; Kubiak, C. P. Self-Assembled Monolayers of Dithiols, Diisocyanides, and Isocyanothiols on Gold: 'Chemically Sticky' Surfaces for Covalent Attachment of Metal Clusters and Studies of Interfacial Electron Transfer. *Inorg. Chim. Acta* **1996,** *242* (1-2), 115-124.

67. Shi, S.; Zhang, Y. D.; Ahn, J.; Qin, D. Revitalizing Silver Nanocrystals as a Redox Catalyst by Modifying Their Surface with an Isocyanide-Based Compound. *Chem. Sci.* **2020,** *11* (41), 11214-11223.

68. Ahn, J.; Shi, S.; Vannatter, B.; Qin, D. Comparative Study of the Adsorption of Thiol and Isocyanide Molecules on a Silver Surface by in situ Surface-Enhanced Raman Scattering. *J. Phys. Chem. C* **2019,** *123* (35), 21571-21580.

69. Zhang, Y.; Liu, J. Y.; Ahn, J. W.; Xiao, T. H.; Li, Z. Y.; Qin, D. Observing the Overgrowth of a Second Metal on Silver Cubic Seeds in Solution by Surface-Enhanced Raman Scattering. *ACS Nano* **2017,** *11* (5), 5080-5086.

70. Lin, X.; Lin, S.; Liu, Y. L.; Gao, M. M.; Zhao, H. Y.; Liu, B. K.; Hasi, W.; Wang, L. Facile Synthesis of Monodisperse Silver Nanospheres in Aqueous Solution Via Seed-Mediated Growth Coupled with Oxidative Etching. *Langmuir* **2018,** *34* (21), 6077-6084.

71. Wang, H.; Musier-Forsyth, K.; Falk, C.; Barbara, P. F. Single-Molecule Spectroscopic Study of Dynamic Nanoscale DNA Bending Behavior of HIV-1 Nucleocapsid Protein. *J. Phys. Chem. B* **2013,** *117* (16), 4183-4196.

72. Zhao, L. B.; Zhang, M.; Huang, Y. F.; Williams, C. T.; Wu, D. Y.; Ren, B.; Tian, Z. Q. Theoretical Study of Plasmon-Enhanced Surface Catalytic Coupling Reactions of Aromatic Amines and Nitro Compounds. *J. Phys. Chem. Lett.* **2014,** *5* (7), 1259-1266.

73. Takeyasu, N.; Kagawa, R.; Sakata, K.; Kaneta, T. Laser Power Threshold of Chemical Transformation on Highly Uniform Plasmonic and Catalytic Nanosurface. *J. Phys. Chem. C* **2016,** *120* (22), 12163-12169.

74. Zhang, Q.; Wang, H. Mechanistic Insights on Plasmon-Driven Photocatalytic Oxidative Coupling of Thiophenol Derivatives: Evidence for Steady-State Photoactivated Oxygen. *J. Phys. Chem. C* **2018,** *122* (10), 5686-5697.

75. Zhang, Q. F.; Chen, K. X.; Wang, H. Hot-Hole-Induced Molecular Scissoring: A Case Study of Plasmon-Driven Decarboxylation of Aromatic Carboxylates. *J. Phys. Chem. C* **2021,** *125* (38), 20958-20971.

76. Baffou, G.; Bordacchini, I.; Baldi, A.; Quidant, R. Simple Experimental Procedures to Distinguish Photothermal from Hot-Carrier Processes in Plasmonics. *Light-Sci. Appl.* **2020,** *9* (1), 108.

77. Rigor, J.; Kurouski, D.; Large, N., Plasmonic Heating Effects in Tip-Enhanced Raman Spectroscopy (TERS). *J. Phys. Chem. C* **2022,** *126* (34), 13986-13993.

TOC Graphic:

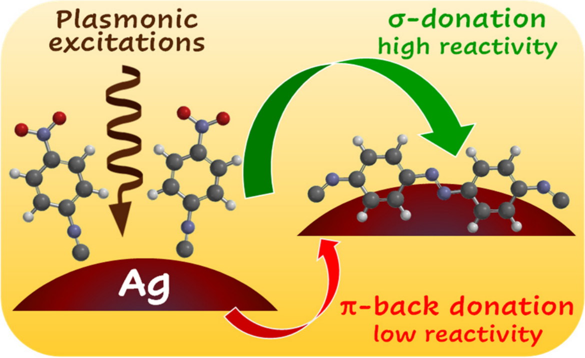
Plasmonic excitations
σ-donation
high reactivity
Ag
π-back donation
low reactivity